First-Principles Investigation of Ti_2CSO and Ti_2CSSe Janus MXene Structures for Li and Mg Electrodes

Edirisuriya M. Dilanga Siriwardane and Jianjun Hu*

Department of Computer Science and Engineering, University of South Carolina, Columbia, SC 29201

E-mail: jianjunh@csc.sc.edu

Abstract

While lithium battery electrodes are constantly being improved in terms of their performance, discovering new materials with alternative energy carriers such as Mg is important to lower the cost of production and to enhance the energy density. MXenes are a type of highly investigated materials with promising energy applications due to their excellent electronic conductivity and good mechanical and dynamical stability. Previous experimental studies showed Janus MoSSe nanosheets provide promising performance for battery electrodes. However, it is not fully understood how MXenes with different surface terminations affect the electrochemical properties and the diffusion barriers of ions. Here we address this problem by studying Ti_2CSO and Ti_2CSSe Janus MXenes for Li and Mg electrodes. Our density functional theory-based, first-principles calculations indicate that both monolayers are thermodynamically, mechanically, and dynamically stable. We calculated that the average voltages for Li and Mg adsorbed Ti_2CST (T = O, Se) MXenes are approximately 0.95 and 0.2 V, respectively. The maximum voltage for Ti_2CSTLi_x is about 2 V, and that for Ti_2CSTMg_x is around

0.45 V. The Mg adsorbed Ti_2CSO monolayer exhibits the highest gravimetric capacity (524.54 mAh/g) compared to that of other Janus MXenes considered in this paper. For $Ti_2CSSeLi_x$, we obtained a higher capacity (230.45 mAh/g) and a lower diffusion barrier (0.191 eV) than that of most of the Li adsorbed S-functionalized MXenes.

Keywords

MXenes, Janus structures, 2D electrodes, Batteries

Introduction

Modern portable devices and electric vehicles are increasingly demanding high-performance, high-energy density storage materials with fast rechargeable capabilities. So far, lithium-ion batteries (LIBs) have been the fundamental energy source of those devices due to the high energy-density and power-density. However, the lack of Li sources, high production cost, and safety issues are significant drawbacks of LIBs. To address these issues, a vast amount of research has been carried out to find alternative energy carriers for rechargeable batteries.[1–5] Among various types of ions, Mg ions attracted enormous attention due to their bivalency which offers high energy-density. The cost of production of energy storage can also be reduced by utilizing Mg because of its high abundance.[1,2]

The two-dimensional (2D) materials have become very popular as reliable electrode materials for energy storage. Their large specific surface areas offer a higher number of electrochemically active sites to store ions compared to that of bulk counterparts. This allows 2D electrodes to have enhanced capacities. Due to the reduced distance between those active sites in the nanosheets, fast charging and discharging rates can be achieved[6,7] while good power densities can be also be obtained. MXene is a large family of 2D materials with a general chemical formula of $M_{n+1}X_nT_x$ where M is an early transition metal atom, X represents C or/and N atom, and T indicates the surface termination.[8,9] The most common

surface terminations reported for MXenes are O, OH, F, and S. It is found that O and S terminated MXenes have better electrochemical properties for battery applications relative to the OH and F functionalized MXenes. The main advantage of $M_{n+1}X_nS_x$ MXenes over $M_{n+1}X_nO_x$ monolayers is that the former has lower diffusion barriers than the latter.[10,11] It is reported that Ti_2CS_2 monolayers exhibit significantly higher gravimetric capacity for Mg compared to that of Ti_2CO_2 nanosheets.[3]

Recently, Janus materials, where the two surfaces functionalized with two different chemical species, were studied for varies applications.[6,12–16] In these new materials, the out-plane-symmetry is broken due to the two distinct surfaces. In 2017, Janus MoSSe was successfully synthesized by Zhang et al.[17] by substituting the top Se layer of $MoSe_2$ with S atoms. It was theoretically suggested that MoSSe has small diffusion barrier (0.24 eV) and high capacity (776.5 mAh/g) for Li-ions.[16,18] Later, MoSSe, TiSSe and VSSe Janus materials were investigated for Na and K electrodes.[15,16] The tunable electronic, magnetic and mechanical properties of Janus MXnese structures were also reported in previous research.[12–14,19]

We find that Janus MXene structures have not been studied for battery electrodes so far. In order to introduce Janus structures for energy applications, we selected Ti_2C nanosheet. Due to the light-weight of this MXene, we can expect a good gravimetric capacity from a functionalized Ti_2C monolayer. Li and Mg were selected as the energy carrier of the electrodes. We first investigated the stability of Ti_2C functionalized with S and O, and also S and Se. Our calculations show that bare Ti_2CST (T = O, Se) MXenes are thermodynamically, mechanically, and kinetically stable. Li adsorbed Ti_2CST monolayers exhibit capacities larger than that of $M_2CS_2Li_x$ MXenes with M= Zr, Hf, V, Nb, Ta, Cr, Mo, and W. Ti_2CSOLi_x provides the capacities greater than that of $M_2NS_2Li_x$ where M=Ti and V. The voltage profiles of Li adsorbed Ti_2CST MXenes provide the average voltages around 1 V, and maximum voltages about 2 V. The average voltages of Ti_2CSTMg_x electrodes are less than 0.3 V, while maximum voltages are around 0.45 V. The lowest diffusion barrier was obtained for $Ti_2CSSeLi_{0.0625}$, which is around 0.191 eV. Moreover, our *ab initio* molecular

dynamic simulations evidence that MXenes with two Li/Mg ion layers are stable at 400 K temperature.

Computational Methods

The density functional theory (DFT) calculations were carried out based on the Vienna *ab initio* simulation package (VASP).[20–23] The projected augmented wave (PAW) pseudopotentials with 500 eV plane-wave cutoff energy were considered for the electron-ion interactions.[24,25] The exchange-correlation functional was treated by using the generalized gradient approximation (GGA) using the Perdew-Burke-Ernzerhof (PBE) method.[26,27] The energy convergence criterion and the force convergence criteria were set as 10^{-5} eV and 10^{-2} eV/Å, respectively. The Γ-centered Monkhorst-Pack k-meshes were used for the Brillouin zone integration of the unit cells. We employed PHONOPY code[28] to assist our phonon dispersion calculations. We performed *ab initio* molecular dynamic (MD) simulations at 400 K temperature to see the stability of Ti_2CSTA_2 (A = Li, Mg) MXenes. $4 \times 4 \times 1$ supercell structures of Ti_2CST monolayers were considered for both phonon and *ab initio* MD computations. The climbing image nudged elastic band (CI-NEB) method was used to calculate the diffusion barrier using VASP transition state tools.[29,30] The calculations in this paper did not consider the van der Waals (vdW) interactions. In the Supporting Information, we compared the results with and without vdW interactions. The vdW calculations were carried out using DFT+D3 with Becke-Jonson damping.[31,32] It is clear that the results do not change considerably under vdW interactions.

Results and Discussion

Properties of bare-Ti_2CST (T = O, Se) Monolayers

Ti_2CST Janus MXenes have two different surface atoms. Those are S and O, or S and Se. By considering the distinct nature of two surfaces and hexagonal crystal symmetry, we identify that bare Ti_2CSO and Ti_2CSSe MXenes can have four different candidate structures. As shown in Fig. 1, we label them as FCC, HCP, HF1 and HF2. In FCC structures, O/Se and S atoms align with Ti atoms, while those surface atoms align with C atoms in HCP structures. O/Se atoms are placed right above Ti atoms and S atoms reside right under C atoms in HF1 structures. On the contrary, O/Se atoms locate on top of C atoms and S atoms locate below Ti atoms in HF2 structures. FCC, HF1 and HF2 systems have P3m1 (156) space-group symmetry, whereas HCP has C1m1 (8). The relative total energy for each structure is mentioned in Table 1. It is clear that both monolayers have FCC ground state structures while HCP exhibits the largest energy. This reflects that the preferable sites of both S and O/Se atoms are located right above the Ti atoms. The top and bottom views of the minimum energy structure are shown in Fig. 2. According to previous studies, Ti_2CO_2 and Ti_2CS_2 MXenes also have FCC as the minimum energy structure.[33,34]

The lattice constant (a) of Ti_2CSO MXene is 3.106 Å and that of Ti_2CSSe MXene is 3.214 Å. The thickness (t) of the MXenes in out-of-plane direction were calculated as the distance between S and O/Se surfaces. The thicknesses of Ti_2CSO and Ti_2CSSe MXene are 5.000 and 5.684 Å, respectively. It is clear that Ti_2CS_2 has a and t values which are almost equal to the respective values of Ti_2CSSe MXene (see Table 2). As a consequence of having the shortest lattice constant and thickness, Ti_2CO_2 has the lowest volume of the functionalized Ti_2C materials in Table 2. This could be because of lower atomic radius of O relative to S and Se and higher attraction between Ti and O in Ti_2CO_2 as proved by the short Ti-O bond lengths and high charge transfer of Ti and O.

Bader charge transfer analysis[35] was done for examining the charge transfer between

Table 1: The relative total energy per unit formula (E) of each candidate structure in eV and the formation energy of ground state structure (E_{form}) in eV/atom.

MXene	E_{FCC}	E_{HCP}	E_{HF1}	E_{HF2}	E_{form}
Ti_2CSO	0	1.32	0.47	0.74	-1.57
Ti_2CSSe	0	1.10	0.41	0.65	-1.56

atoms (see Table 2). C, S and O atoms of the MXenes gained electrons as indicated by the negative charge transfer. On the contrary, Ti lost electrons since the charge transfer values are positive. C is able to gain higher number of electrons because each C atom is surrounded by six Ti atoms. Table 2 shows that the Ti-Se bond length is considerably greater than the Ti-O bond length. This can be attributed to the higher charge transfer from Ti to O compared to that from Ti to Se, and also the lower atomic radius of O relative to that of Se. Thus, the Ti-O bonds are much stronger than the Ti-Se bonds due to the higher electronegativity of O compared to that of Se. In contrast Ti-S and Ti-C bond lengths, which are common to both materials, do not show much difference.

To study the thermodynamic stability of Ti_2C MXenes functionalized with S and O, or S and Se, we calculated the formation energy based on Eq. 1. Here, $E[Ti_2CST]$ is the total energy of Ti_2CST monolayer, $E[Ti_2C]$ is the total energy of Ti_2C MXene, $E[S]$ represents the total energy of S atom in its bulk material and $E[T]$ is the total energy of Se (O) atom in their bulk (gas) compounds. As shown in Table 1, E_{form} values are negative for both materials indicating synthesizing these materials are highly possible. We also carried out spin polarized DFT calculations to investigate the magnetic nature of the structures. DFT provides zero magnetic moment for each atom of the unit cells implying that the nonmagnetic ground states are very stable.

$$E_{\text{form}} = \frac{1}{5}(E[Ti_2CST] - E[Ti_2C] - E[S] - E[T]) \tag{1}$$

The elastic constants were extracted from the DFPT calculations as shown in Table 2. Due to the hexagonal symmetry of MXenes, C_{11} and C_{22} are equal to each other. The

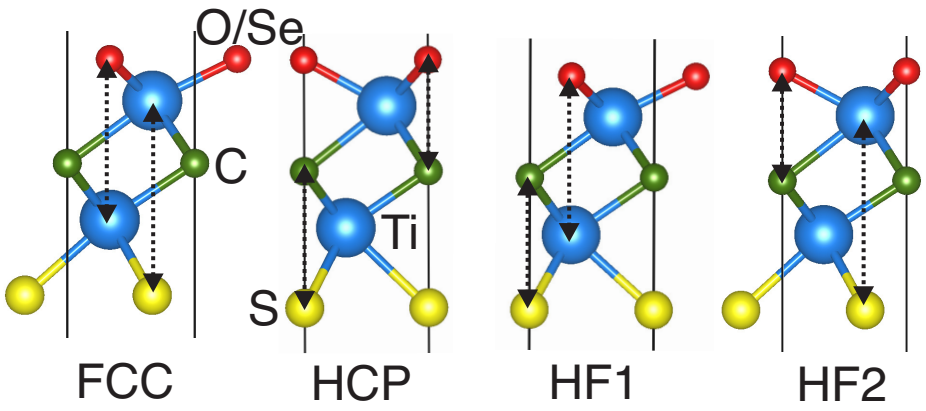

Figure 1: The side views of candidate structures for bare Ti_2CST MXenes

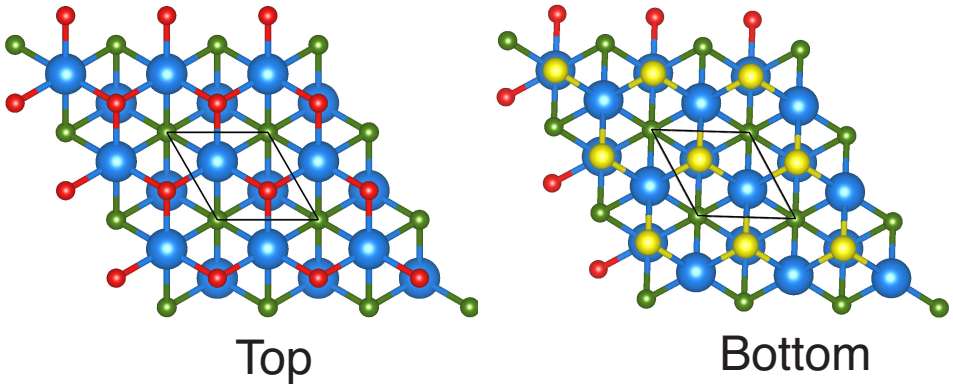

Figure 2: The top and bottom views of ground-state structure (FCC) of bare Ti_2CST MXenes

Table 2: The lattice constant (a), thickness (t), Ti-S, Ti-T (T = O, Se), Ti-C bond lengths, C_{11} and C_{12} elastic constants, Yong's modulus (Y) and Poisson's ratio (ν) of Ti_2CST MXenes.

MXene	a (Å)	t (Å)	Ti-S (Å)	Ti-T (Å)	Ti-C	C_{11} (GPa)	C_{12} (GPa)	Y (GPa)	ν	Δq_C (e)	Δq_{Ti} (e)	Δq_S (e)	Δq_T (e)
Ti_2CSO	3.106	5.000	2.402	2.000	2.229	433.45	137.91	389.57	0.318	-2.229	2.372	-0.980	-1.328
Ti_2CSSe	3.214	5.684	2.398	2.568	2.181	248.34	143.26	165.70	0.577	-2.335	2.110	-1.035	-0.851
Ti_2CS_2 [33]	3.197	5.521	2.406	-	2.211	337.62	104.39	305.35	0.309	-1.843	1.739	-0.814	-
Ti_2CO_2 [34,36]	3.037	4.431	-	1.976	2.189	627.03	196.49	565.00	0.312	-1.746	2.028	-	-1.155

obtained values are $C_{11} = 433.45$ GPa and $C_{12} = 137.91$ GPa for Ti_2CSO , while $C_{11} = 248.34$ GPa and $C_{12} = 143.26$ GPa for Ti_2CSSe. It is clear that both materials comply with the stability conditions of the hexagonal monolayers. Those conditions are $C_{11} > 0$, $C_{11} - C_{12} > 0$ and $C_{11} > |C_{12}|$.[6,37,38] The positive phonons in the phonon calculations in Fig. 3 (a) and (b) show that both monolayers are dynamically stable at 0K temperature.

Moreover, we calculated the Young's modulus (Y) and Poisson's ratio (ν) based on Eq. 2 and 3.[36] Y of Ti_2C decreases as $Y(Ti_2CO_2) > Y(Ti_2CSO) > Y(Ti_2CS_2) > Y(Ti_2CSSe)$. This relationship indicates that the higher bond strength of T-O than that of Ti-S and Ti-Se, significantly affects the stiffness of the materials. Due to the smaller ν values of Ti_2CO_2, Ti_2CS_2, and Ti_2CSO than that of Ti_2CSSe, the resistance produced against strain by those three monolayers are higher than that from Ti_2CSSe.

$$Y = \frac{(C_{11}^2 - C_{12}^2)}{C_{11}} \tag{2}$$

$$\nu = \frac{C_{12}}{C_{11}} \tag{3}$$

As can be seen in Fig.3 (c) and (d), the density of states (DOS) crosses the Fermi-level, which is marked by zero energy line. This confirms that both monolayers are metallic. In Ti_2CSO DOS plot (see Fig.3 (c)), the Ti-d orbitals significantly dominate near the Fermi-level, while the p orbitals of the all the atoms contribute almost equally. However, the contribution from both Ti-d and C-p states are significant for the DOS of Ti_2CSSe MXenes (see Fig.3 (d)). Since considerable amount of DOS of Ti-d orbitals present near the Fermi-level, we can expect a good metallic-character in both materials, which is important for an

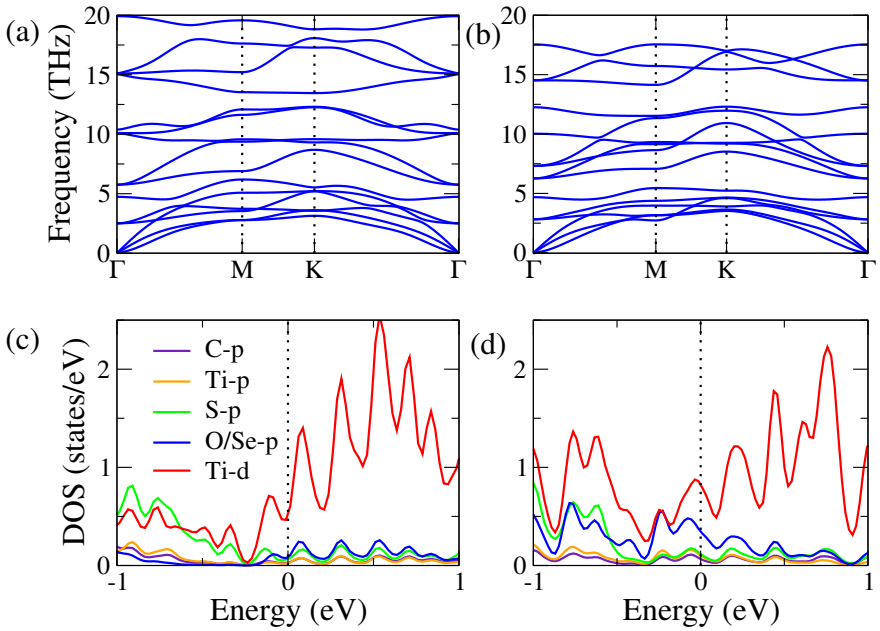

Figure 3: The projected density of states (PDOS) of (a) Ti_2CSO and (b) Ti_2CSSe MXenes, and also phonon dispersion curves of (c) Ti_2CSO and (d) Ti_2CSSe MXenes.

excellent electrode material.

Single Ion Adsorption

In order to study the effects on a single Li/Mg ion, we created 4×4 supercells of Ti_2CST MXenes ($Ti_2CSTLi_{0.0625}$). We found four different sites for introducing an ion to the systems. Those are labeled as S1, S2, S3, and S4, as shown in Fig.4. Here, the sites S1 and S2 exist on the O-layer or Se-layer, while S3 and S4 are placed on the S-layer. The Li-ions on S1 and S4 are aligned with a C atom, and S2 and S3 are right above or under a Ti atom.

We calculated the binding energy of the Li atoms at each site based on Eq. 4. Here, $E(M_2CS_2{+}nA)$ is the total energy of a Ti_2CST MXene, which adsorbs n number of A=Li/Mg ions. $E(M_2CS_2)$ indicates the total energy of bare-MXene, and $E(A)$ is the energy of a Li/Mg atom.

$$E_b = \frac{1}{n}[E(M_2CS_2 + nA) - E(M_2CS_2) - nE(A)] \tag{4}$$

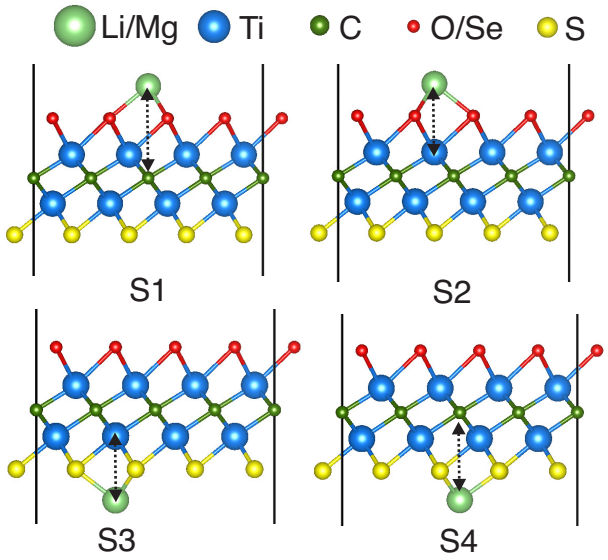

Figure 4: The side views of the candidate structures for single ion adsorbed Ti_2CST MXenes

It is clear from Fig.5 that the binding energies of all the sites are negative, indicating Li can be adsorbed at any of the locations. The single Li/Mg ion prefers to locate at the S2 site of Ti_2CSO MXene, where S2 is at the O-surface. In Ti_2CSSe MXene, the preferable sites are at S-surface, i.e., S3 is for Li and S4 is for Mg.

We carried out charge transfer and bond length analysis to study the atomic properties' effects on the binding energy. We calculated the average charge transfer of the surface atoms (η), which form bonds with Li/Mg ions. For instance, η = O for S1 site of Ti_2CSO MXene and η = S for S3 site of the same material. As can be seen in Fig 5, the magnitudes of Bader charge transfer (Δq_η) of those η atoms are maximum at the sites where binding energy of Li is minimum. The $\eta-$Li and $\eta-$Mg bond lengths are minimum at the sites which provide the lowest binding energies. Therefore, higher Coulomb interactions exist at the sites with low binding energies. The low binding energy of ions is preferable for electrodes since it prevents forming bulk Li and Mg compounds. Thus, this structure-binding energy relationship shows that ionic-interaction is one of the most important factors behind the stability of the Li/Mg ions adsorbed on the MXenes.

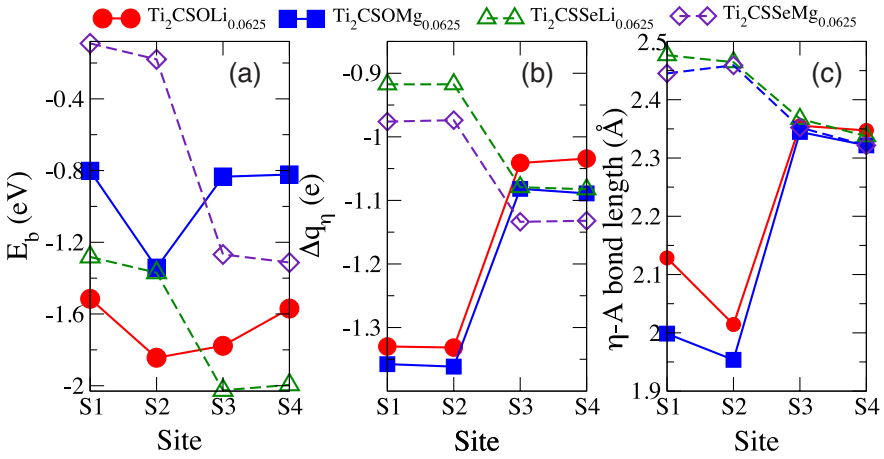

Figure 5: (a) Binding energy of Li/Mg ion, (b) average Bader charge transfer (Δq) of the surface atoms (η) where Li/Mg ion resides, and (c) η-ion(A) bond length as a function of site.

Table 3: The table contains the in-plane strain (Δa) and out-of-plane strain (Δt) on single ion adsorbed and two-ion layers adsorbed MXenes as percentages, maximum voltages ($V_{\max}$), average voltage (V_{avg}), gravimetric capacity (C_{g})

MXene	Δa (%) single-ion	Δa (%) full coverage	Δt (%) single-ion	Δt (%) full coverage	$V_{\max}$(V)	V_{avg1}(V)[1]	V_{avg2}(V)[2]	C_{g} (mAh/g)
Ti_2CSOLi_x	-0.16	0	0.280	6.75	2.000	0.950	1.017	315.94
Ti_2CSOMg_x	-0.13	1.20	-0.16	7.24	0.429	0.193	0.154	524.54
$Ti_2CSSeLi_x$	0.03	4.10	-0.67	-2.22	1.912	0.945	0.854	230.45
$Ti_2CSSeMg_x$	0.27	2.32	-0.17	-1.22	0.493	0.207	0.286	345.22

1. V_{avg1} was calculated by using $V_{\text{avg1}} = \frac{\sum_i^N V_i}{N}$ expression, where V_i is the positive voltages in Fig. 8 (b) and N is the number of positive voltage steps.
2. V_{avg2} was calculated by using Eq.6, where $x_1 = 0$ and $x_2 = x_{\max}$

Multiple Ions Adsorption

Next, we considered the effects of multiple ions adsorption on Ti_2CST MXene. The most challenging task of this step is that finding the ground state of electrodes with different Li/Mg ion concentrations. Most of the research on 2D material electrodes considered large supercells to find the energies of materials with multiple ions. But there is a high possibility that one can select the wrong Li arrangement on the supercell as the minimum energy configuration. That can generate inaccurate voltage profiles and maximum capacities. Recently, alloy-theoretic automated toolkit (ATAT)[39] was used to search the minimum energy ion configurations

of the electrodes.[33,40,41] ATAT code generates numerous structural candidates for a given composition by adopting an automatic cluster expansion method. Finally, the minimum energy candidates are found with the aid of VASP.

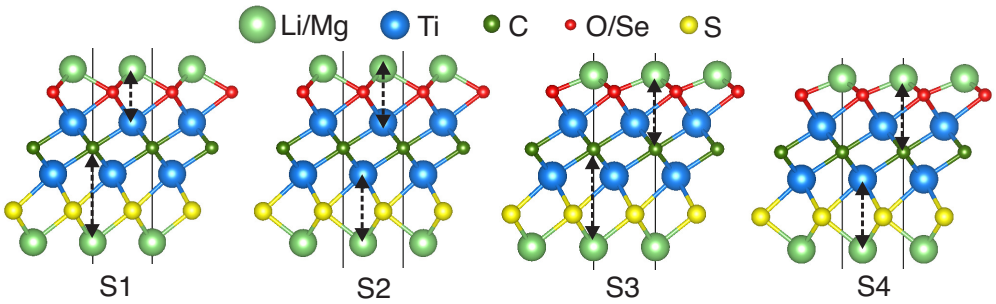

Figure 6: The side views of the candidate structures for Ti_2CSTA_2 (A=Li/Mg) MXenes

ATAT recognizes low energy structures between two given compositions. In our work, we considered the unitcells of Ti_2CST and Ti_2CSTA_2 (A = Li/Mg) as the structures with low-ion and high-ion concentrations. Our goal is to find $Ti_2CSTA_{2-2\alpha}$ structures with different Li/Mg contents (α) to investigate the binding energies and open-circuit voltage as a function of ion content. We carried out the ground state search for different Li-contents until the cross-validation score becomes less than 0.02 eV. As a result of having two distinct surfaces on Ti_2CST MXenes, we can identify four different candidate structures for Ti_2CSTA_2 by placing the ions at different sites, as shown in Fig. 6. Those four configurations are labeled as S1, S2, S3, and S4. In the S1 structure, the ion on the O/Se surface is placed above the nearest Ti atom, and the ion on the S surface is located below the C atoms. Both ions are aligned with Ti (C) atoms for the S2 (S3) structures. In the S4 configuration, the ion on the O/Se surface is located above C atoms, and the other ion is aligned with the nearest Ti atom. According to our calculations S4 is the preferred structure for Ti_2CSOLi_2, and that for Ti_2CSOMg_2 and $Ti_2CSSeLi_2$ is S3. S2 was found as the minimum configuration for $Ti_2CSSeMg_2$.

In ATAT, the formation energies (E'_{form}) for the generated compositions are calculated based on Eq. 5. $E[Ti_2CSTA_x]$, $E[Ti_2CST]$, and $E[Ti_2CSTA_2]$ are the total energy of Ti_2CST with x content of A (Li/Mg) ions, ion free Ti_2CST, and Ti_2CSTA_2, respectively. In Fig.7, the most stable compounds have the lowest formation energies. Both Ti_2CSOLi_x and

Ti_2CSOMg_x MXenes have minimum formation energies at $x = 1$. The lowest energies for $Ti_2CSSeLi_x$ and $Ti_2CSSeMg_x$ MXenes are found at $x = 0.72$ and $x = 0.66$, respectively. The lower formation energies of Li adsorbed materials than that of Mg electrodes indicate that Ti_2CSTLi_x MXenes provide more stable phases compared to Ti_2CSTMg_x MXenes.

$$E'_{\text{form}} = \frac{1}{2}(2E[\text{Ti}_2\text{CSTA}_x] - (2-x)E[\text{Ti}_2\text{CST}] - xE[\text{Ti}_2\text{CSTA}_2]) \tag{5}$$

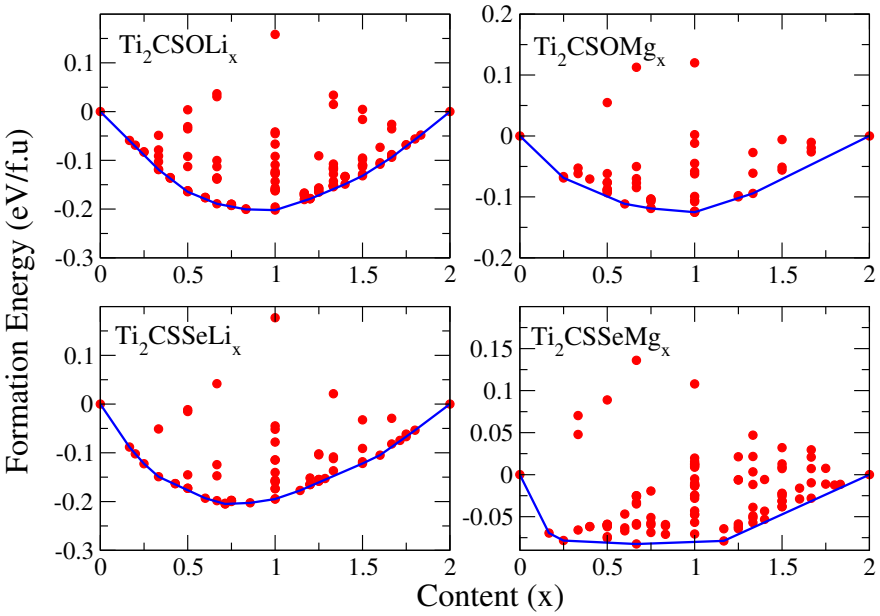

Figure 7: The formation energy calculated by ATAT for Ti_2CSTA_x structures as a function of Li/Mg ion content (x). The blue lines indicate the thermodynamically stable compositions at 0K temperature.

Furthermore, we calculated the binding energy of Li/Mg ions as a function of ion content using Eq. 4 as shown in Fig. 8. It is clear that the binding energy rises when the ion content increases. This is mainly due to the enhanced repulsion between the ions when multiple ions are adsorbed on the monolayers. Both Li adsorbed Ti_2CSO, and Ti_2CSSe MXenes provide lower binding energies compared to that of Mg adsorbed counterparts. Those results agree with the formation energies calculated by cluster expansion, where the Li-based electrodes provided lower values compared to that from the Mg-based electrodes. Thus, we can expect the high stability of Li relative to Mg on those nanosheets.

To study the strain (Δa) induced by Li adsorption, we calculated Δa based on the expression $\Delta a = \frac{(a-a_0)\times 100}{a_0}$. Here, a_0 is the lattice constant of the bare-MXene, and a is the lattice constant of Li/Mg adsorbed material. We calculated the strains of the single ion adsorbed monolayers ($Ti_2CSTA_{0.0625}$) and the MXenes with double Li/Mg ion layers (Ti_2CSTA_2). It is clear from Table 3 that Δa is negligible for all the electrodes when a single ion is adsorbed. All the strains are less than 0.3 % for $Ti_2CSTA_{0.0625}$ compounds. But, Δa is considerable or negligible depending on the type of A and T atoms. Surprisingly, Ti_2CSOLi_2 has no strain found. On the contrary, Δa is around 1.2 % for Ti_2CSOMg_2. $Ti_2CSSeLi_2$ exhibits the largest Δa (4.1 %) in Table 3. $Ti_2CSSeMg_2$ shows $\Delta a \approx 2.3$ %. Thus we can expect very low surface expansion in Ti_2CSO MXenes compared to Ti_2CSSe MXenes. We also computed the out-of-plane strain (Δt) by determining the thickness of the MXenes, as shown in Table 3. Even though the in-plane strain is very low in Ti_2CSOA_2 monolayers, the out-of-plane strain is considerable. On the contrary, Δt values of Ti_2CSSeA_2 MXenes is more than three times lower than that of O-based counterparts.

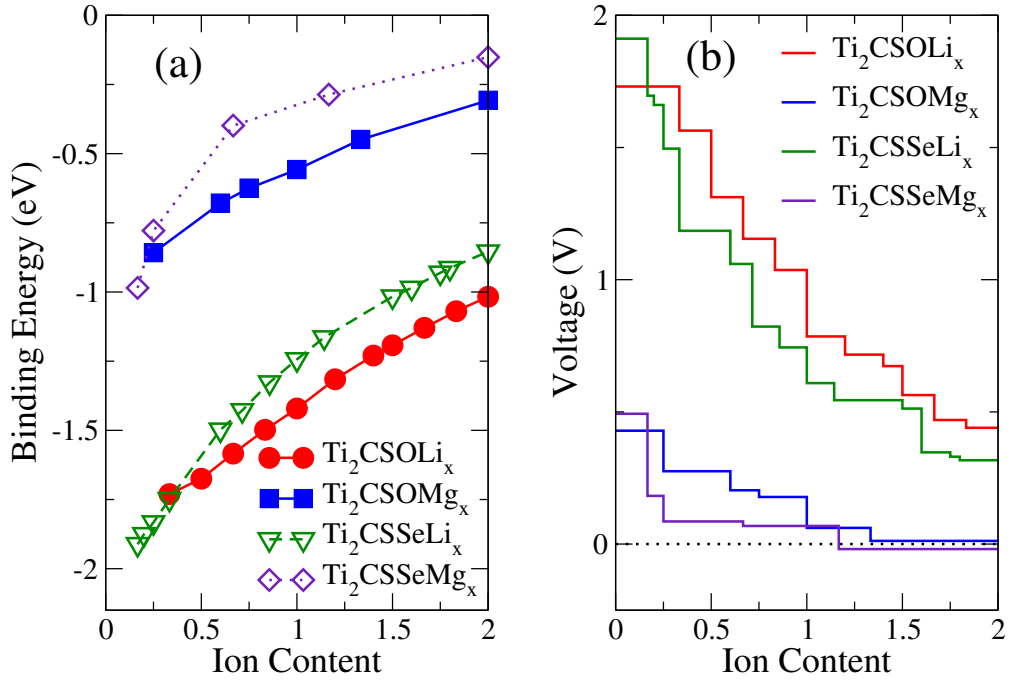

Figure 8: The binding energy of Li and Mg ions of Ti_2CSTA_x (A=Li/Mg) MXenes

As will be explained later, Ti_2CSOLi_2, Ti_2CSOMg_2 and $Ti_2CSSeLi_2$ are thermodynami-

cally stable. Therefore, we carried *ab-initio* MD simulations using VASP to investigate the stability of those materials at high temperatures. Our MD simulations were performed based on the isothermal-isobaric (NPT) ensemble at 400 K temperature, which is way higher than the room temperature. The MD simulations were carried out with 4×4 supercells for 5 ps. The total energy and the temperature variations in Fig. 9 suggest that those materials are stable at 400 K. This provides the evidence that Ti_2CSOLi_2, $Ti_2CSSeLi_2$ and Ti_2CSOLi_2 MXenes can exist at room temperature. We did not observe any bond breaking or formation of Li_xS.

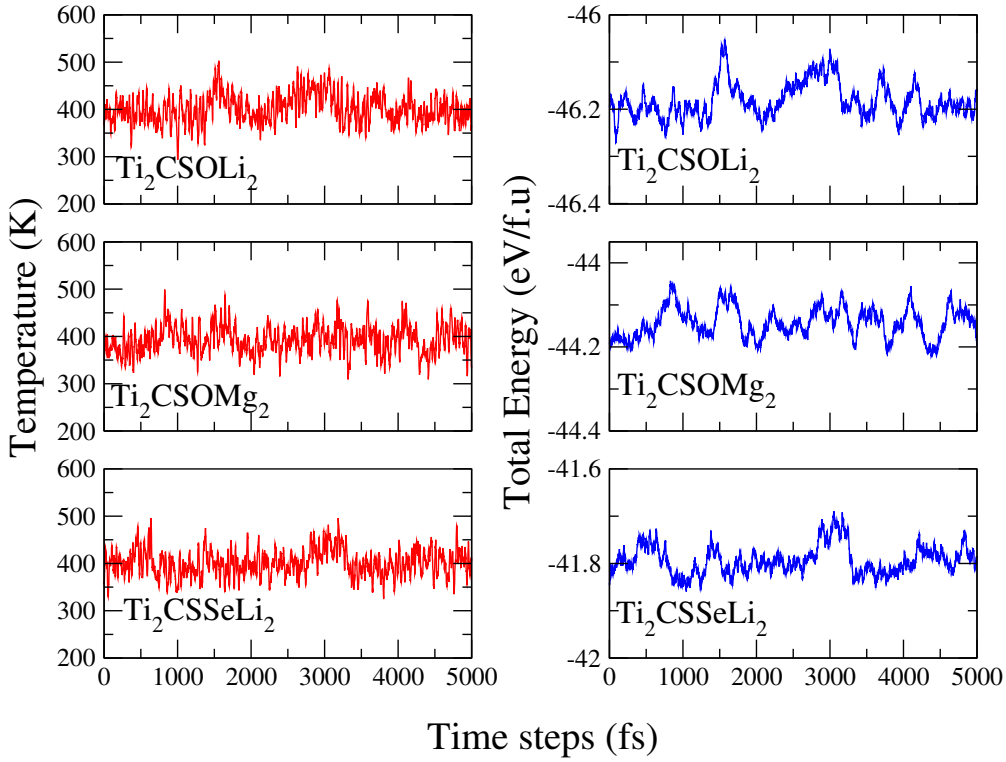

Figure 9: The temperature and total energy variations of Ti_2CSTA_x (A=Li/Mg) MXenes in MD simulations at 400 K.

Electrochemical Properties

We investigated the voltage profiles of the Ti_2CSTA_x MXenes based on the following chemical reaction,

$$(x_2 - x_1)\mathrm{A}^{z+} + (x_2 - x_1)e^- + \mathrm{Ti_2CSTA}_{x_1} \leftrightarrow \mathrm{Ti_2CSTA}_{x_2},$$

where z is the valency. $z = 1$ and $z = 2$ for Li and Mg, respectively. The open-circuit voltage for the above reaction is the Gibbs free energy ($G(x)$) which is defined as $G(x) = \Delta E + P\Delta V' - T\Delta S$. Here, ΔE is the internal energy change (computing from the DFT simulations at T= 0K), P is the pressure, $\Delta V'$ is the volume change, T indicates the temperature and ΔS represents the entropy change of the system. We can neglect $P\Delta V'$ and $T\Delta S$ terms, since those quantities are approximately equal to 10^{-5} eV and 25 meV, respectively.[33] As a result, voltage can be determined calculating $G(x)$ using the total energy (E) of $\mathrm{Ti_2CSTA}_{x_1}$, $\mathrm{Ti_2CSTA}_{x_2}$, and A atoms, as shown in Eq.6.

$$V \approx \frac{E(\mathrm{Ti_2CSTA}_{x_1}) - E(\mathrm{Ti_2CSTA}_{x_2}) + (x_2 - x_1)E(A)}{z(x_2 - x_1)e} \tag{6}$$

We plotted the voltage profiles for $\mathrm{Ti_2CSTA}_x$ MXenes as a function of x as shown in Fig. 8. For the whole range of ion content (x = 0 - 2), the Li electrodes has much higher voltages compared to their Mg counter parts. Table 3 provides the average (V_{avg}) and maximum (V_{max}) voltages of each electrode. V_{max} of both Li electrodes are around 2 V and V_{avg} values lie between 0.85-1.017 V. Li adsorbed $\mathrm{Ti_2CS_2}$ also provide about 2 V as V_{max} and around 1 V as V_{avg}.[33] V_{avg} of Li adsorbed $\mathrm{Ti_2NS_2}$ is around 0.64 V, which is smaller than that of $\mathrm{Ti_2CS_2}$ and Ti$_2$CST MXenes.[5] V_{avg} voltages of Ti$_2$CST monolayers are greater than that of $\mathrm{M_2CS_2}$ MXenes, where M = V, Nb, Ta, Cr, Mo and W.[33] Mg adsorbed Ti$_2$CST electrodes exhibit 4 times smaller maximum values ($\approx$ 0.4 - 0.5 V) relative to Li adsorbed that electrodes. V_{avg} of Mg adsorbed structures are very small, which are less than 0.3 V. The previous studies also reported that Mg adsorbed S-functionalized Ti$_2$C MXenes have very low voltages. Mg adsorbed Ti$_2$CSO and Ti$_2$CSSe electrodes provide approximately the same average voltage (0.2V) as that of $\mathrm{Ti_2CS_2}$ monolayers (0.1 V).[3] Thus, by functionalizing single or both sides of Ti$_2$C MXenes with S, we can expect low voltages for Mg electrodes. Those Mg electrodes

can be suitable as anodes to keep high voltage differences in batteries.

As illustrated by Fig.8 (b), full two layers of Li can be stored on both Janus MXenes, since the voltage is positive from 0 to 2 ion content. However, only Ti_2CSO monolayer can adsorb two Mg layers. The maximum Mg ion content for Ti_2CSSe was computed as 1.67. To further investigate the storage properties, we determined the gravimetric capacity based on the following equation,

$$C_g = \frac{x_{\max} \times z \times F \times 10^3}{M}, \tag{7}$$

where M is the mass of Ti_2CSTA_x with maximum Li/Mg content ($x = x_{\max}$) and F is the Faraday constant (26.81 Ah/mol). As illustrated by Table. 3, Ti_2CSOMg_x electrode shows the largest C_g value, which is 524.54 mAh/g. This is mainly due to the bivalency of the Mg ion where it donates two electrons per ion. The double Mg layers adsorbed Ti_2CO_2 electrodes exhibit a higher capacity (570 mAh/g) than that of Ti_2CSO.[4] Ti_2CSOLi_x electrode provides a capacity around 315.94 mAh/g, which is greater than the capacity provided by $Ti_2CS_2Li_x$ (288.6 mAh/g). It should also report that Ti_2CSOLi_x, Ti_2CSOMg_x, and $Ti_2CSSeLi_x$ electrodes have higher capacities than $Ti_2NS_2Li_x$ (308.28 mAh/g) and $V_2NS_2Li_x$ MXenes (299.52 mAh/g).[5] All four electrodes reported in Table. 3 have capacities greater than that of $M_2CS_2Li_x$ MXenes, where M= Zr, Hf, V, Nb, Ta, Cr, Mo and W.[33] It has been reported that Ti_2CS_2 has a significantly higher capacity for Mg-ions (1871.13 mAh/g) than that of Ti_2CSO and Ti_2CSSe electrodes. On the contrary, those three electrodes have approximately equal capacities for Li-ions.[3]

Diffusion Barrier

Next, we calculated the diffusion barriers (E_{diff}) of Li/Mg adsorbed $Ti_2CSTA_{0.0625}$ MXenes using the CI-NEB method as implemented in VASP. Since there are two different surfaces for each MXene, we calculated E_{diff} of both surfaces, as shown in Fig.10. Here, red lines

indicate the E_{diff} of O/Se surfaces, while blue lines represent that of S-surfaces. As explained previously, Li/Mg ions prefer different locations on Ti_2CST MXenes. Li ions' preferable site is right above a C atom for O-surfaces (i.e., S2), while it provides the minimum energy when Li ion is adsorbed right above a Ti atom (i.e, S3). Even though the minimum energy structures are S2 and S3 for Mg ions in Ti_2CSO, those ions prefer S2 and S4 (S4 is a site right above a C atom on S-surface) sites in Ti_2CSO (see Fig.11). Therefore, we used those minimum energy sites of each surface as the initial and final locations of the ions to calculate the energy barrier.

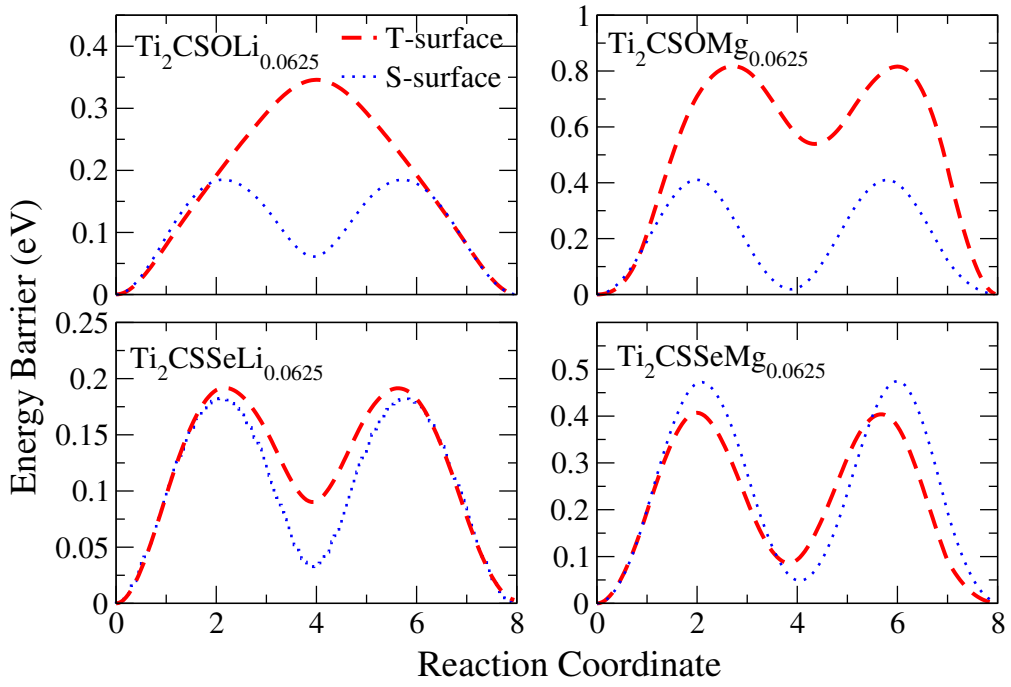

Figure 10: The diffusion barrier (E_{diff}) of single ion adsorbed 4×4 super-cells of Ti_2CST MXenes. The broken red lines represent the T(O/Se)-surface and blue lines are for S-surface.

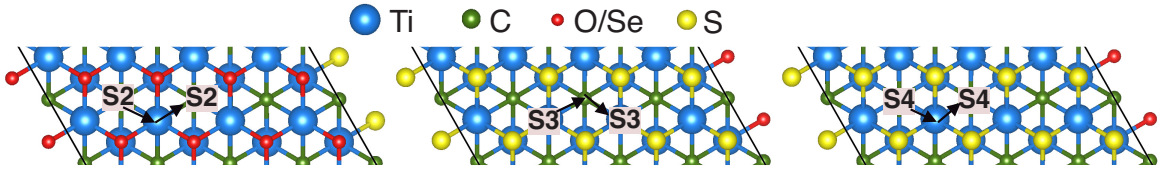

Figure 11: Diffusion paths for A (Li/Mg) on $Ti_2CSTA_{0.0625}$ MXenes. For $Ti_2CSOLi_{0.0625}$ and $Ti_2CSOMg_{0.0625}$ and $Ti_2CSSeLi_{0.0625}$, S2 and S3 are the minimum energy sites on O- and S-surfaces, respectively. For $Ti_2CSSeMg_{0.0625}$, S2 and S4 are the minimum energy sites.

On Ti_2CSO monolayers, there are significant differences between E_{diff} of O-surface and that of S-surface as illustrated by Fig.10. This can be possibly due to the considerable electronegativity difference between S and O. Li and Mg ions strongly interact with O ions because of the high electronegativity of O. Instead, S and Se have similar electronegativities. Thus, E_{diff} of a Li/Mg ion is almost equal on both surfaces of Ti_2CSSe monolayer. E_{diff} found for Li on O-surface of Ti_2CSO is around 0.34 eV and that on S-surface is 0.18 eV. Mg shows exceptionally higher E_{diff} (0.71 eV) as a result of bivalency of Mg ions. Ti_2CSSe monolayer also evidences that Mg has a higher barrier by exhibiting 0.47 eV maximum E_{diff} which is twice the value found for Li-ions on the same monolayer. E_{diff} of $Ti_2CSSeMg_{0.0625}$ is approximately equal to that of $Ti_2CS_2Mg_{0.0625}$.[3] It is reported that a single Mg ion adsorbed 4×4 supercells of Ti_2CO_2, and $Ti_3C_2O_2$ monolayers show E_{diff} greater than 0.6 eV, which is higher than that of $Ti_2CSSeMg_{0.0625}$.[4] $Ti_2CSSeLi_{0.0625}$ provides lower E_{diff} than that of $M_2CS_2Li_{0.0625}$ MXenes, where M = Zr, Hf, V, Nb and Ta.[33] Due to the low E_{diff} in Li adsorbed Ti_2CST, we can expect higher charging and discharging rates.

Conclusion

We performed density functional theory based first-principles studies to examine how MXenes with different surface terminations affect the stability, electrochemical properties, and diffusion barriers of Ti_2CSO and Ti_2CSSe Janus MXenes for Li and Mg electrodes. We proved that both Janus structures are thermodynamically stable when Ti_2C MXenes are functionalized with S and O/Se. The phonon calculations indicate that Ti_2CST structures are dynamically stable at 0 K temperature. The elastic constants of both MXenes comply with the criteria for mechanical stability. The density of states plots of those Janus structures have metallic character while the region near the Fermi level is rich with Ti-d orbitals. This can offer good electronic conduction for the electrodes. The in-plain strain of the two Li/Mg layers adsorbed Ti_2CSO MXenes is very small, while the out-of-plane strain

is around 7 %. Ti_2CSSe monolayers with two Li/Mg layers show strains between 2 % - 4 %, whereas out-of-plane strain is less than 0.7 %. The *ab initio* MD calculations show that Ti_2CSOLi_2, Ti_2CSOMg_2 and $Ti_2CSSeLi_2$ structures are stable at 400 K temperature. The average voltages of Li adsorbed Janus MXenes are found as ≈ 0.95 V, and those of Mg adsorbed monolayers are ≈ 0.2 V. The theoretical capacities of the Janus MXenes are greater than 230 mAh/g, which are higher than the capacities of Li adsorbed M_2CS_2 monolayers with M = Zr, Hf, V, Nb, Ta, Cr, Mo, and W. Ti_2CSSe nanosheets show lower diffusion barrier compared to those of Ti_2CSO MXenes. $Ti_2CSSeLi_{0.0625}$ exhibits the lowest diffusion barrier (0.191 eV), which is lower than those of the 2D M_2CS_2 electrodes, where M = Zr, Hf, V, Nb, Ta, Mo, and W.

Acknowledgment

Research reported in this work was supported in part by NSF under the grants 1940099 and 1905775. The views, perspective, and content do not necessarily represent the official views of the NSF.

Supporting Information

- The lattice constants and thicknesses of bare-Ti_2CST MXenes using DFT+D3 method.
- The in-plane and and out-of-plane strains of Ti_2CSTA_2 MXenes using DFT+D3 method.
- The average voltages and gravimetric capacities using DFT+D3 method.
- The energy barrier using DFT+D3 method.

References

1. Xu, M.; Lei, S.; Qi, J.; Dou, Q.; Liu, L.; Lu, Y.; Huang, Q.; Shi, S.; Yan, X. Opening Magnesium Storage Capability of Two-Dimensional MXene by Intercalation of Cationic Surfactant. *ACS Nano* **2018**, *12*, 3733–3740, PMID: 29543438.

2. Zhao, M.-Q.; Ren, C. E.; Alhabeb, M.; Anasori, B.; Barsoum, M. W.; Gogotsi, Y. Magnesium-Ion Storage Capability of MXenes. *ACS Appl. Energy Mater.* **2019**, *2*, 1572–1578.

3. Wang, Y.; Zhou, M.; Xu, L.-C.; Zhao, W.; Li, R.; Yang, Z.; Liu, R.; Li, X. Achieving superior high-capacity batteries with the lightest Ti2C MXene anode by first-principles calculations: Overarching role of S-functionate (Ti 2CS2) and multivalent cations carrier. *J. Power Sources* **2020**, *451*, 227791.

4. Xie, Y.; Dall'Agnese, Y.; Naguib, M.; Gogotsi, Y.; Barsoum, M. W.; Zhuang, H. L.; Kent, P. R. C. Prediction and Characterization of MXene Nanosheet Anodes for Non-Lithium-Ion Batteries. *ACS Nano* **2014**, *8*, 9606–9615, PMID: 25157692.

5. Shukla, V.; Jena, N. K.; Naqvi, S. R.; Luo, W.; Ahuja, R. Modelling high-performing batteries with Mxenes: The case of S-functionalized two-dimensional nitride Mxene electrode. *Nano Energy* **2019**, *58*, 877 – 885.

6. Jin, W.; Wu, S.; Wang, Z. Structural, electronic and mechanical properties of two-dimensional Janus transition metal carbides and nitrides. *Physica E Low Dimens. Syst. Nanostruct.* **2018**, *103*, 307 – 313.

7. Rojaee, R.; Shahbazian-Yassar, R. Two-Dimensional Materials to Address the Lithium Battery Challenges. *ACS Nano* **2020**, *14*, 2628–2658, PMID: 32083832.

8. Anasori, B.; Lukatskaya, M. R.; Gogotsi, Y. 2D Metal Carbides and Nitrides (MXenes) for Energy Storage. *Nat. Rev. Mater.* **2017**, *2*, 16098.

9. Sun, Y.; Chen, D.; Liang, Z. Two-Dimensional MXenes for Energy Storage and Conversion Applications. *Mater. Today Energy* **2017**, *5*, 22 – 36.

10. Zhu, J.; Chroneos, A.; Eppinger, J.; Schwingenschlögl, U. S-functionalized MXenes as electrode materials for Li-ion batteries. *Appl. Mater. Today* **2016**, *5*, 19 – 24.

11. Li, Y.-M.; Guo, Y.-L.; Jiao, Z.-Y. The effect of S-functionalized and vacancies on V2C MXenes as anode materials for Na-ion and Li-ion batteries. *Curr Appl Phys* **2020**, *20*, 310 – 319.

12. Akgenc, B. Intriguing of two-dimensional Janus surface-functionalized MXenes: An ab initio calculation. *Comput. Mater. Sci.* **2020**, *171*, 109231.

13. He, J.; Lyu, P.; Sun, L. Z.; Morales Garcìa, A.; Nachtigall, P. High temperature spin-polarized semiconductivity with zero magnetization in two-dimensional Janus MXenes. *J. Mater. Chem. C* **2016**, *4*, 6500–6509.

14. Jin, W.; Wu, S.; Wang, Z. Structural, electronic and mechanical properties of two-dimensional Janus transition metal carbides and nitrides. *Physica E Low Dimens.* **2018**, *103*, 307 – 313.

15. Xiong, F.; Chen, Y. A first-principles study of Janus monolayer TiSSe and VSSe as anode materials in alkali metal ion batteries. *Nanotechnology* **2020**, *32*, 025702.

16. Wang, H.; Chen, Q.; Li, H.; Duan, Q.; Jiang, D.; Hou, J. Two-dimensional Janus MoSSe as a potential anode material for Na/K-ion batteries: A theoretical study. *Chemical Physics Letters* **2019**, *735*, 136777.

17. Zhang, J.; Jia, S.; Kholmanov, I.; Dong, L.; Er, D.; Chen, W.; Guo, H.; Jin, Z.; Shenoy, V. B.; Shi, L. *et al.* Janus Monolayer Transition-Metal Dichalcogenides. *ACS Nano* **2017**, *11*, 8192–8198, PMID: 28771310.

18. Shang, C.; Lei, X.; Hou, B.; Wu, M.; Xu, B.; Liu, G.; Ouyang, C. Theoretical Prediction of Janus MoSSe as a Potential Anode Material for Lithium-Ion Batteries. *J. Phys. Chem. C* . **2018**, *122*, 23899–23909.

19. Frey, N. C.; Bandyopadhyay, A.; Kumar, H.; Anasori, B.; Gogotsi, Y.; Shenoy, V. B. Surface-Engineered MXenes: Electric Field Control of Magnetism and Enhanced Magnetic Anisotropy. *ACS Nano* **2019**, *13*, 2831–2839.

20. Kresse, G.; Hafner, J. ab initio. *Phys. Rev. B* **1993**, *47*, 558–561.

21. Kresse, G.; Hafner, J. ab initio. *Phys. Rev. B* **1994**, *49*, 14251–14269.

22. G. Kresse, J. F. Efficiency of ab initio Total Energy Calculations for Metals and Semiconductors Using a Plane-Wave Basis Set. *Comput. Mater. Sci.* **1996**, *6*, 15–50.

23. Kresse, G.; Furthmüller, J. Efficient Iterative Schemes for ab initio Total-Energy Calculations Using a Plane-Wave Basis Set. *Phys. Rev. B* **1996**, *54*, 11169–11186.

24. Blöchl, P. E. Projector Augmented-Wave Method. *Phys. Rev. B* **1994**, *50*, 17953–17979.

25. Kresse, G.; Joubert, D. From Ultrasoft Pseudopotentials to the Projector Augmented-Wave Method. *Phys. Rev. B* **1999**, *59*, 1758–1775.

26. Perdew, J. P.; Burke, K.; Ernzerhof, M. Generalized Gradient Approximation Made Simple. *Phys. Rev. Lett.* **1996**, *77*, 3865–3868.

27. Perdew, J. P.; Burke, K.; Ernzerhof, M. Generalized Gradient Approximation Made Simple [Phys. Rev. Lett. 77, 3865 (1996)]. *Phys. Rev. Lett.* **1997**, *78*, 1396–1396.

28. Togo, A.; Tanaka, I. First principles phonon calculations in materials science. *Scr. Mater.* **2015**, *108*, 1–5.

29. Henkelman, G.; Uberuaga, B. P.; Jónsson, H. A Climbing Image Nudged Elastic Band Method for Finding Saddle Points and Minimum Energy Paths. *J. Chem. Phys.* **2000**, *113*, 9901–9904.

30. Henkelman, G.; Jónsson, H. Improved Tangent Estimate in the Nudged Elastic Band Method for Finding Minimum Energy Paths and Saddle Points. *J. Chem. Phys.* **2000**, *113*, 9978–9985.

31. Grimme, S.; Antony, J.; Ehrlich, S.; Krieg, H. A consistent and accurate ab initio parametrization of density functional dispersion correction (DFT-D) for the 94 elements H-Pu. *The Journal of Chemical Physics* **2010**, *132*, 154104.

32. Grimme, S.; Ehrlich, S.; Goerigk, L. Effect of the damping function in dispersion corrected density functional theory. *Journal of Computational Chemistry 32*, 1456–1465.

33. Siriwardane, E. M. D.; Demiroglu, I.; Sevik, C.; Peeters, F. M.; Çakır, D. Assessment of Sulfur-Functionalized MXenes for Li-Ion Battery Applications. *J. Phys. Chem. C* . **2020**, *124*, 21293–21304.

34. Guo, Z.; Zhou, J.; Si, C.; Sun, Z. Flexible two-dimensional Tin+1Cn (n = 1, 2 and 3) and their functionalized MXenes predicted by density functional theories. *Phys. Chem. Chem. Phys.* **2015**, *17*, 15348–15354.

35. Yu, M.; Trinkle, D. R. Accurate and efficient algorithm for Bader charge integration. *J. Chem. Phys.* **2011**, *134*, 064111.

36. Khaledialidusti, R.; Anasori, B.; Barnoush, A. Temperature-dependent mechanical properties of Tin+1CnO2 (n = 1, 2) MXene monolayers: a first-principles study. *Phys. Chem. Chem. Phys.* **2020**, *22*, 3414–3424.

37. Thomas, S.; Ajith, K.; Lee, S. U.; Valsakumar, M. C. Assessment of the mechanical

properties of monolayer graphene using the energy and strain-fluctuation methods. *RSC Adv.* **2018**, *8*, 27283–27292.

38. Wang, V.; Xu, N.; Liu, J.; Tang, G.; Geng, W. VASPKIT: A User-friendly Interface Facilitating High-throughput Computing and Analysis Using VASP Code. 2019.

39. van de Walle, A.; Asta, M.; Ceder, G. The alloy theoretic automated toolkit: A user guide. *Calphad* **2002**, *26*, 539 – 553.

40. Xu, H.; Xiao, W.; Wang, Z.; Hu, J.; Shao, G. Self-consistent assessment of Li+ ion cathodes: Theory vs. experiments. *J. Energy Chem.* **2021**, *59*, 229 – 241.

41. Wang, Q.; Gu, F.; Xie, Y.; Shui, M.; Shu, J. In-depth lithium transportation mechanism and lithium intercalation study of BaLi2Ti6O14 anode material by atomistic simulations. *J. Electroanal. Chem.* **2020**, *879*, 114790.

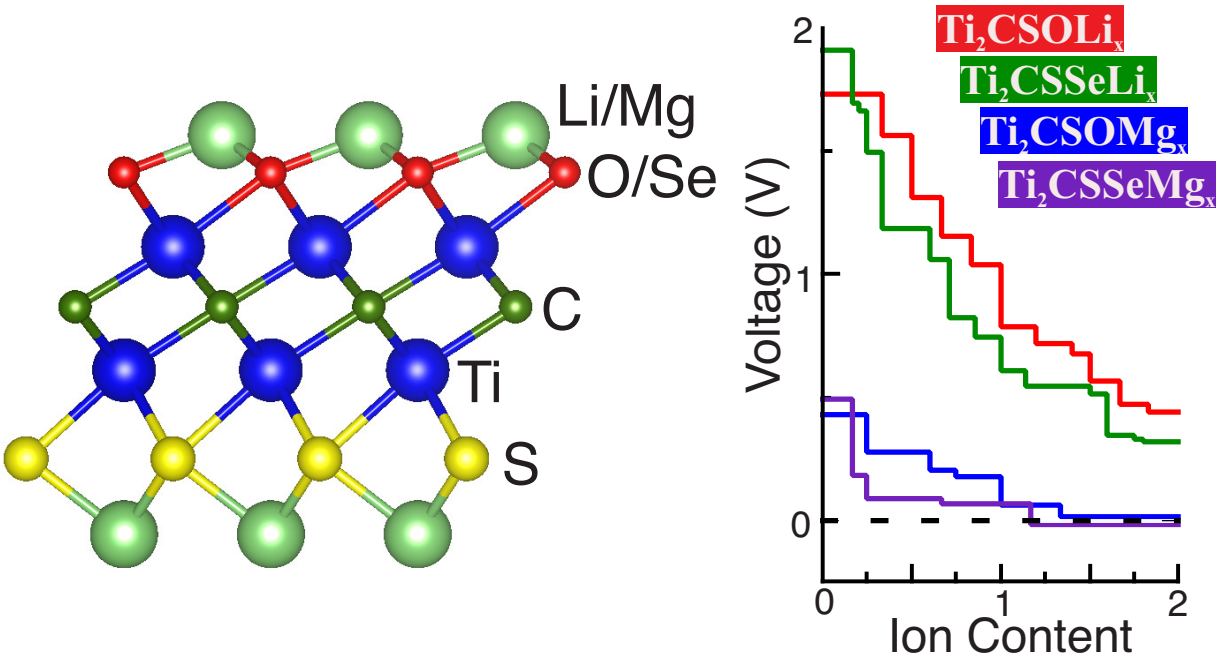

Figure 12: Table of Contents Graphic